Technology in Cancer Research & Treatment
ISSN 1533-0346
Volume 4, Number 5, October (2005)

Optical Biopsy of Lymph Node Morphology using Optical Coherence Tomography

www.tcrt.org

Wei Luo, M.S.[1,§]
Freddy T. Nguyen, B.A., B.S.[1,2,§]
Adam M. Zysk, M.S.[1,3,§]
Tyler S. Ralston, M.S.[1,3]
John Brockenbrough, M.D.[4]
Daniel L. Marks, Ph.D.[1,3]
Amy L. Oldenburg, Ph.D.[1,3]
Stephen A. Boppart, M.D., Ph.D.[1,5,*]

[1]Beckman Institute for Advanced Science and Technology
[2]Department of Chemistry
Medical Scholars Program
College of Medicine
[3]Department of Electrical and Computer Engineering
[4]Carle Foundation Hospital
College of Medicine
[5]Department of Electrical and Computer Engineering
Department of Bioengineering
Colleges of Engineering and Medicine.

University of Illinois at Urbana-Champaign
Beckman Institute for Advanced Science and Technology
405 N. Mathews Ave.
Urbana, IL 61801, USA

§Authors have contributed equally to this work.

* Corresponding Author:
Stephen A. Boppart, M.D., Ph.D.
Email: boppart@uiuc.edu

Optical diagnostic imaging techniques are increasingly being used in the clinical environment, allowing for improved screening and diagnosis while minimizing the number of invasive procedures. Diffuse optical tomography, for example, is capable of whole-breast imaging and is being developed as an alternative to traditional X-ray mammography. While this may eventually be a very effective screening method, other optical techniques are better suited for imaging on the cellular and molecular scale. Optical Coherence Tomography (OCT), for instance, is capable of high-resolution cross-sectional imaging of tissue morphology. In a manner analogous to ultrasound imaging except using optics, pulses of near-infrared light are sent into the tissue while coherence-gated reflections are measured interferometrically to form a cross-sectional image of tissue. In this paper we apply OCT techniques for the high-resolution three-dimensional visualization of lymph node morphology. We present the first reported OCT images showing detailed morphological structure and corresponding histological features of lymph nodes from a carcinogen-induced rat mammary tumor model, as well as from a human lymph node containing late stage metastatic disease. The results illustrate the potential for OCT to visualize detailed lymph node structures on the scale of micrometastases and the potential for the detection of metastatic nodal disease intraoperatively.

Key words: Lymph node; Optical coherence tomography; Optical imaging; High-resolution imaging; Metastasis; and Breast cancer.

Introduction

Breast Cancer

Breast cancer continues to be one of the most frequently diagnosed cancers among women and the second leading source of cancer deaths in women. According to the most recent American Cancer Society statistics, approximately 211,240 new cases (or 32% of all new cancer cases amongst women) of invasive breast cancer and 58,490 new cases of *in situ* breast cancer are expected to be reported in the U.S. in 2005 (1). The number of U.S. deaths attributed to breast cancer this year is estimated at 40,870, second only to lung cancer (1). Over the years, the decrease in the number of breast cancer deaths has largely been attributed to increased awareness, earlier detection, and improved treatment.

There is a continued emphasis on the early diagnosis of breast cancer in order to provide better managed care. The ability to detect and remove a tumor prior to metastasis is essential to lowering the breast cancer mortality rate. The survival

Abbreviations: ALND, Axillary Lymph Node Detection; MNU, *N*-methyl-*N*-nitrosourea; NIR, Near Infrared; OCT, Optical Coherence Tomography; SLNB, Sentinel Lymph Node Biopsy.

rate for U.S. breast cancer patients when the disease is detected at a localized stage is currently 97.5% (2). However, according to the American Cancer Society statistics, approximately 37% of the newly reported breast cancer cases in the U.S. are diagnosed at later stages when the tumor is no longer localized (2).

One major method currently used to detect metastatic breast disease is axillary lymph node dissection (ALND). It is well known that as cancer cells metastasize from the primary tumor site they often travel through the lymphatic system as part of the natural immunological mechanism for processing and filtering out abnormal cells and foreign bodies. Cancerous cells tend to aggregate and cause the reactive enlargement of lymph nodes located near the primary tumor site and downstream in the lymphatic drainage pattern. In breast cancer patients, the two most common patterns drain into the axillary nodes (88-100%) and the internal mammary chain region (10-52%) and are highly dependent on the location of the primary breast cancer (3). In the past, it was common for a patient to undergo a complete axillary lymph node resection in order to histologically analyze all of the nodes suspected to contain metastases. Standard axillary lymph node dissection led to the removal of 10-30 lymph nodes and often adjacent non-diagnostic tissue. This extensive surgical procedure frequently resulted in a number of post-operative long-term complications such as numbness, sensitivity, and lymphedema in the dissection area and extremity.

A more recent and less complicating surgical procedure is the sentinel lymph node biopsy (SLNB) (4). This technique has revolutionized the management of melanoma and solid tumors that metastasize through the lymphatic system (5, 6). The sentinel lymph node is the first node in the lymphatic drainage pattern leading away from the tumor site. This diagnostic procedure drastically reduces the number of lymph nodes removed in the axillary area to one to three nodes and eliminates the need for a complete ALND for patients with a negative SLNB. In addition to providing an equally valid diagnosis (7), reducing the patient's discomfort, and decreasing the associated costs, the SLNB has been shown in a number of clinical studies to be an effective method for the staging of breast cancer especially in assessing whether the cancer has metastasized to the axillary lymph nodes (7). An accurate staging of the metastatic state is the single most predictive factor of 10- and 20-year patient survival (8).

The SLNB is performed using techniques to aid in the mapping of the breast lymphatic system and the identification of the sentinel node. One method is the use of a radioactive tracer, technetium-99, and a dye, methylene blue, to locate the sentinel nodes (8). A small dose of the technetium-99 is injected into the breast along with the blue dye and allowed to circulate through the lymphatic system for a period of 30 minutes to 8 hours (8). The dye aids in the visualization of node location and the level of radioactivity is used as a diagnostic marker to guide the removal of the entire lymph node. Although these can be used individually, a lower rate of false negatives is achieved when combined. Other traditional lymphatic mapping methods include standard X-ray and computed tomography (CT). Recent developments in contrast agents such as near-infrared (NIR) quantum dots (9) and indocyanine green (ICG) dye (10) allow for a more accurate visualization of sentinel lymph node location. Magnetic resonance imaging (MRI) contrast agents such as G6 (11) have also been recently demonstrated in mouse models yielding 3-D lymphatic drainage maps. Similar to the methylene blue dye, these contrast agents take an extended period of time to propagate through the lymphatic system.

Once a lymph node has been identified and resected, a pathological assessment is made to determine its status, thereby assessing disease progression, a process referred to as staging. OCT may provide beneficial alternatives to current methods for lymph node assessment, and subsequently affect the staging procedure. OCT is a low-cost and minimally invasive technique that is capable of imaging morphological structures at cellular resolutions as well as identifying the location of lymph nodes in tissue without the use of radioactive tracers or dyes. In comparison to other optical biomedical imaging techniques, OCT is also capable of imaging 2-3 mm in depth in opaque samples, allowing for the real-time *in vivo* evaluation of the tissue prior to its resection.

Optical Coherence Tomography

Optical coherence tomography is a nondestructive optical imaging modality that uses NIR light to form cross-sectional images of tissue morphology (12). Light reflected from structures within the tissue is coherence-gated to form a depth-resolved image of the specimen, in much the same way that ultrasound images are formed using acoustic pulses. OCT, however, has achieved resolutions approaching that of conventional histopathology and is able to resolve cellular features due to the very short wavelengths in the optical regime and the precision afforded by interferometric detection (Figure 1) (13). The ability to acquire high resolution *in vivo* images may lead to the use of OCT to perform optical biopsies without the need for tissue excision or resection (14).

Since its introduction in 1991, OCT has undergone rapid growth, extending across a wide range of applications in medical and laboratory research. Commercially available equipment is now in widespread clinical use by ophthalmologists for the imaging of retinal pathologies and other ocular diseases (15). OCT imaging of more dense scattering tissues (16) has yielded a wide array of potential applications. In order to achieve imaging depths of 2-3 mm in non-transpar-

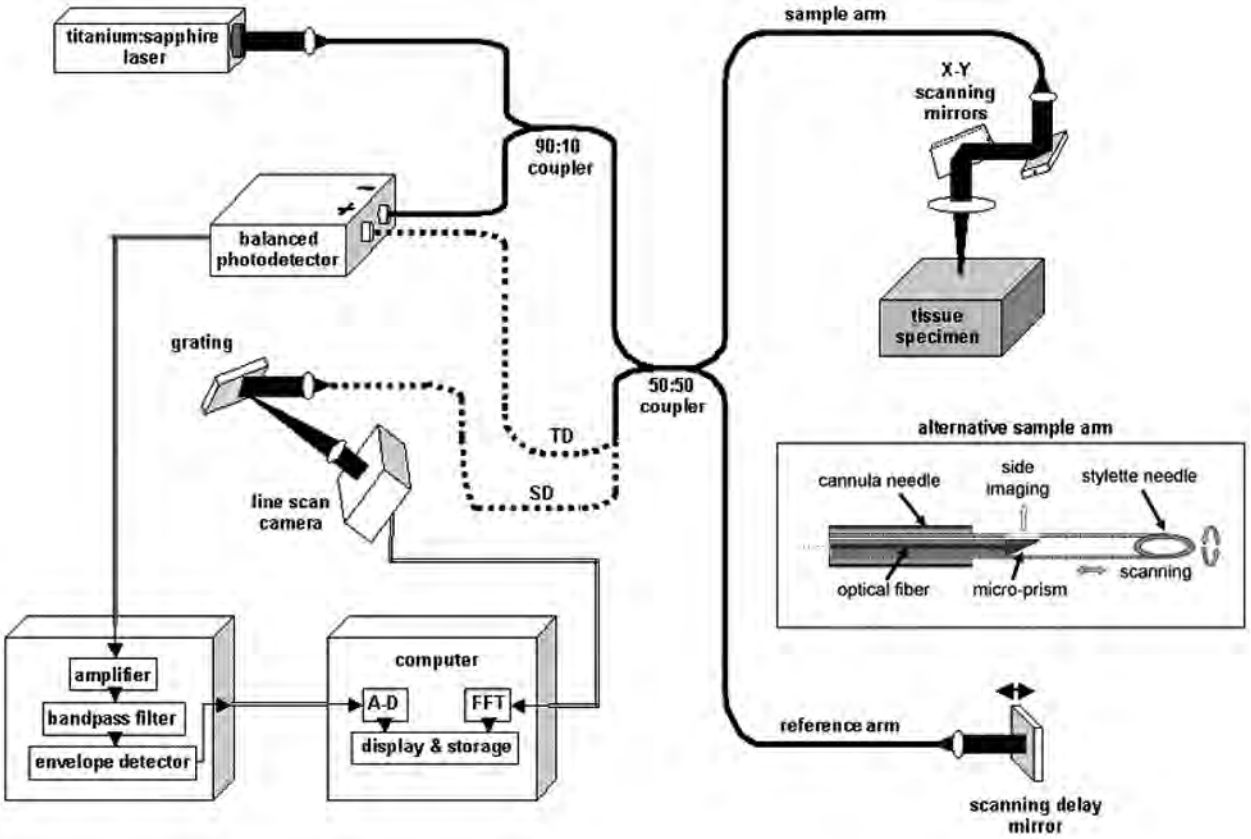

Figure 1: Schematic illustrating a fiber-optic-based OCT system. The small size and portability of this system makes it appropriate for use in clinical, surgical, and research settings. The alternative sample arm configuration shows an OCT probe used in conjunction with a core-needle or fine-needle aspiration biopsy device allowing for *in vivo* imaging of subsurface structures. Both time-domain (TD) and spectral domain (SD) detection schemes are included. **Abbreviations:** A-D, Analog-to-digital converter; FFT, Fast Fourier transform.

ent samples, these applications take advantage of the natural "biological window" that exists in tissue, a portion of the NIR optical spectrum approximately between 700-1300 nm where absorption is minimal and attenuation is largely due to scattering effects (17, 18). High resolution OCT imaging has been demonstrated in the fields of dermatology (19, 20), cardiology (21-23), neurology (24, 25), gynecology (26, 27), and gastroenterology (28, 29), among many others.

OCT is also a highly robust and adaptable imaging modality. Advances in broadband optical sources have yielded OCT axial resolutions of less than 2 μm (30-32). Real-time imaging has also been reported, using either swept-source optical frequency domain imaging (OFDI) or broadband spectral domain (SD) systems with axial scan-line rates of up to 29,000 per second (33-35). Capabilities such as Doppler analysis (36, 37) and polarization sensitivity (38) have been incorporated into OCT systems, as well, enabling the study of blood flow and skin burns, respectively. Contrast agents have also been developed, adding molecular sensitivity to OCT images and thereby enabling the potential detection of chemical disease markers prior to evident morphological changes (39, 40).

OCT imaging systems have been integrated into a variety of modern clinical instruments. In the surgical suite, for exam-

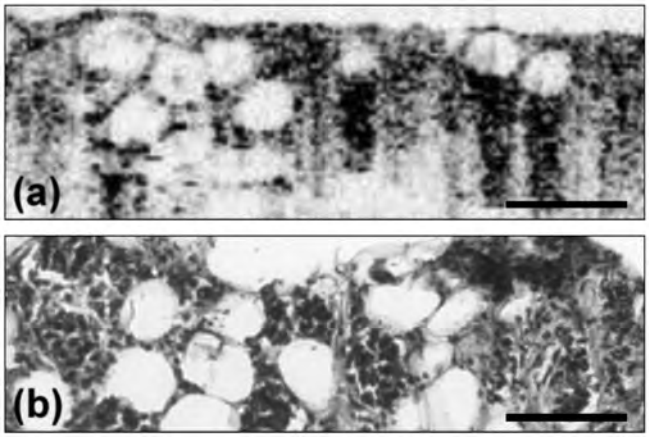

Figure 2: OCT of invasive human ductal carcinoma. Strong correspondence exists between the (**a**) OCT image and the (**b**) corresponding histology in terms of both tissue density and feature locations, most noticeably among the large lipid-filled adipose cells. Images are cropped to facilitate correspondence. Optical attenuation effects in full OCT images of breast tumor tissue allow for typical penetration depths of approximately 1 mm, given the wavelength and incident optical power used in these studies. Pixels in (**a**) are 1 μm square. Scale bars represent 100 μm.

ple, the depth scanning capabilities of OCT have been used to augment the capabilities of standard surgical microscopes (24). Endoscopic, catheter, and needle probes have also been developed, allowing for high resolution analysis of the GI tract and vasculature, or in conjunction with soft tissue biopsy procedures (Figure 1, inset) (13, 41, 42). The potential for OCT imaging in fine- and core-needle breast biopsy procedures, as well as in open surgical biopsy procedures, may offer a powerful tool for the differentiation of normal tissue and neoplastic growth (43). Figure 2 shows a representative OCT image and corresponding histology of a human invasive ductal carcinoma of the breast, captured *ex vivo*. Clear morphological similarities are evident between these images, demonstrating the potential diagnostic value of OCT.

Materials and Methods

Animal Model

A clinically relevant animal model, already being employed in parallel studies, was adopted for this study (44, 45). The induction of mammary tumors of virgin female rats by injection with the direct-acting carcinogen *N*-methyl-*N*-nitrosourea (MNU) is the most widely used animal model for studying breast cancer development (46-48). Mammary carcinogenesis in this model mimics numerous characteristics associated with human breast carcinogenesis, including hormone dependency and histopathological features (46). Invasion of the regional lymph node chain has been observed under this rat model, and distant metastases to the lung have also been reported (46). Similar patterns of invasion and metastasis are observed in the human disease (49). The induced tumors emulate the carcinogenesis of human ductal carcinoma, first as ductal carcinoma *in situ*, then as locally invasive disease, and finally as metastatic disease to the liver, lung, and spleen (43, 44, 48, 50, 51). Using this animal model, we were able to validate the use of OCT for the visualization of microscopic tumor morphology and the identification of tumor margins (43). In this study, we demonstrate the application of OCT as an "optical biopsy" technique for the evaluation of lymph node morphology in this rat tumor model.

All animal procedures were performed according to a protocol approved by the Institutional Animal Care and Use Committee of the University of Illinois at Urbana-Champaign. Female Sprague-Dawley rats were purchased from Harlan (Indianapolis, IN) at three to four weeks of age, individually housed in rooms with controlled temperature and lighting, and fed rodent laboratory chow (Harlan Teklad, Madison, WI). At four weeks and six weeks of age, six rats were administered one dose of MNU (Sigma Chemical, St. Louis, MO; i.p. 55 mg/kg in saline) as part of parallel ongoing studies of carcinogenesis in this tumor model. Two control rats were injected with an equal volume of a saline vehicle. Beginning two weeks post-MNU injection, animals were palpated weekly. Rats that developed mammary masses around 3 cm in size, and corresponding control animals, were euthanized by carbon dioxide asphyxiation prior to OCT imaging. A midline and two lateral incisions were made in the abdominal skin to reflect back the abdominal wall, exposing the peritoneal cavity and the mesenteric lymph nodes. The animals were placed on an OCT microscope stage for initial imaging. Subsequently, the mesenteric lymph nodes were dissected, placed in Petri dishes, and imaged using OCT. All eight animals were imaged for this study with an average of three lymph nodes per animal and 256 OCT images per lymph node.

Human Tissue Specimens

Specimens of surgically-resected human tissue, including two lymph nodes, were provided fresh and stored in 0.9% normal saline after a pathological diagnosis was made. Specimens were imaged using OCT within 24 hours, followed by standard histological processing. Both lymph nodes were imaged in three-dimensions, acquiring a total of 400 cross-sectional OCT images. Tissue procurement and imaging was performed under protocols approved by the Institutional Review Boards of Carle Foundation Hospital, Urbana, Illinois, and the University of Illinois at Urbana-Champaign.

Tissue and Image Analysis

After imaging, tissue was fixed in 10% neutral buffered formalin solution for standard histological processing. Samples were embedded in paraffin and sectioned 5 μm thick with a rotary microtome (RM2255, Leica Microsystems, Inc.). Sections were stained with hematoxylin and eosin (H&E) and prepared on glass slides according to standard protocol for light microscopy observation. Light microscopy was performed (BH-2, Olympus, Japan) and digital images were captured (Spot RT Slider, Diagnostic Instruments) for comparison with OCT images. Image analysis yielded the identification and correlation of microstructural features. The OCT and histological images presented here represent the best match based on the observed architectural morphology. Three-dimensional data sets were constructed and analyzed using commercially available software (Slicer Dicer® 4.0, PIXOTEC) on a personal computer. Three-dimensional projections were generated and rotated along the X-Y-Z coordinates for the visualization of node features.

Optical Coherence Tomography Instrument

The OCT instrument in this study (Figure 1) used light from a neodymium:vanadate pumped titanium:sapphire laser with a center wavelength of 800 nm and a 100 nm bandwidth.

The broad bandwidth yielded an axial imaging resolution of approximately 2 μm in tissue. A 20 mm achromatic lens was used to focus approximately 10 mW of light down to a 15 μm spot size (transverse resolution) onto the sample from a single-mode 50/50 fiber optic splitter (Gould Fiber Optics, Inc.) that also coupled light reflected from a galvanometer-based reference delay operating at a rate of 30 scan lines per second. Spatial scanning in the X-Y plane was accomplished *via* a pair of galvanometer-mounted mirrors (Cambridge Technology, Inc.). Time-domain detection was achieved *via* a dual-balanced detection scheme (52) using a 125 kHz auto-balanced photoreceiver (New Focus Inc., Model #2007) and data acquisition was performed by a dedicated computer cards (National Instruments, Model #PCI-6110, PCI-6711) with a 10MHz sampling rate, a 12-bit quantizer, and a ±5V input range. Data acquisition in the spectral domain was achieved using a diffraction grating with 830 grooves/mm and blazed for 828nm (Richardson Grating Laboratory, Rochester, New York) to disperse the light, and a lens to focus onto a line scan camera (Model #L104K, Basler Vision Technologies). The time domain and spectral domain systems have measured signal-to-noise ratios (SNR) of approximately 100dB and 90dB, at acquisition rates of 10 lines/sec and 29,000 lines/sec, respectively.

The human breast cancer tissue specimen and the rat lymph nodes were both imaged using time-domain OCT (TD-OCT). Recent technological advances have led to the addition of Fourier-domain optical detection in OCT, enabling significantly faster acquisition speeds with minimal corresponding loss of sensitivity. Employing a method referred to as spectral-domain OCT (SD-OCT) (33-35), the same broadband light source was employed and the signal was measured using a spectrometer (see Figure 1).

Results

Mesenteric rat lymph nodes were imaged *in vivo* and *in vitro* using OCT. During three-dimensional OCT imaging, 256 2-D images of each specimen were acquired in 10 μm spatial increments. The images of two representative *in vitro* rat lymph nodes are presented in Figures 3 and 4. Two blocks of 3-D OCT data sets from 256 2-D images each are shown with computational cutouts demonstrating three different cross-sectional planes. Corresponding histological sections are also presented for comparison. Detailed structures are shown in the OCT images in Figure 3, including the lymphoid follicles located at the outer part of the node,

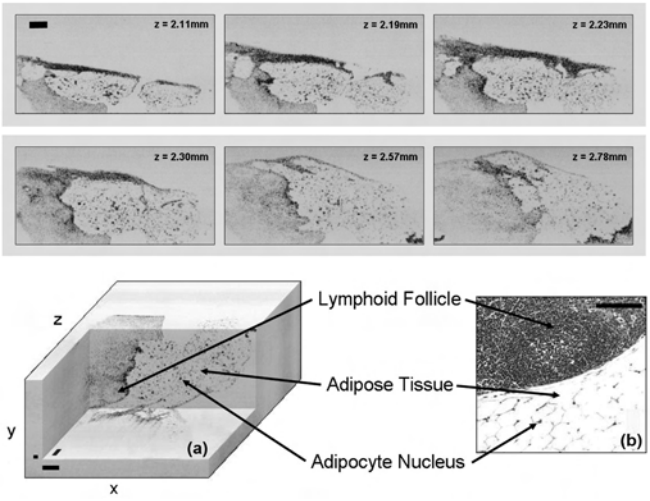

Figure 3: Images of an *in vitro* rat lymph node showing the boundary between mammary adipose tissue and lymph node. *Top*: Sequence of 2-D OCT images through the sample wherein the changing morphology of the node boundary is evident. Visible structures, including adipose tissue and a lymphoid follicle, are well correlated between OCT and H&E-stained histology images. (**a**) Computational cutout of a block extracted from the 3-D OCT data set. (**b**) Corresponding H&E-stained histological section of the sample. The OCT imaging beam was incident from the back-side of the 3-D block in (**a**), and perpendicular to the 2-D OCT images shown above. The lymph node was translated in 10 μm increments in the X-Z plane to acquire each 2-D image comprising the 3-D data set. Pixel dimensions in the 3-D set are 1 μm, 10 μm, and 3 μm in the x, y, and z directions, respectively. Scale bars = 100 μm.

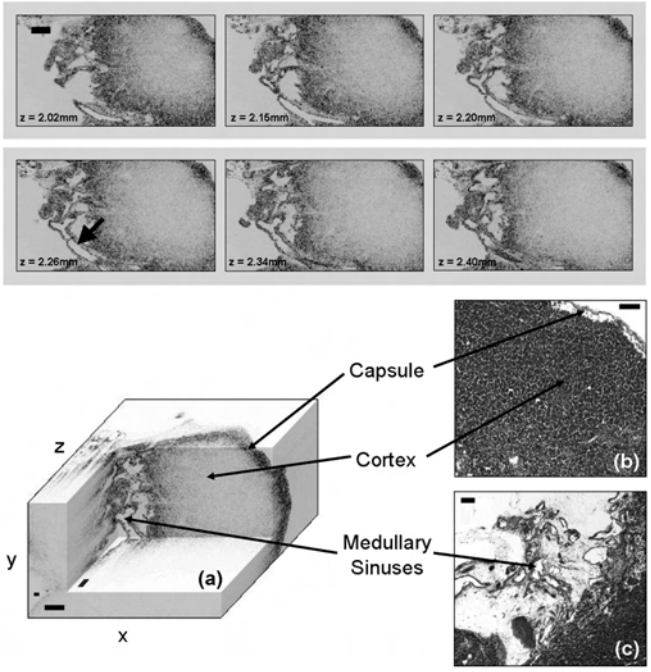

Figure 4: Images of *in vitro* rat lymph node showing internal structures. *Top*: Sequence of 2-D OCT images through the node shows changing morphology of the sinus structure (arrow). Visible structures, including the capsule, cortex, and medullary sinuses, are well correlated between OCT and H&E-stain histology images. (**a**) Computational cutout of a block extracted from the 3-D OCT data set. (**b**,**c**) Corresponding H&E-stained histological sections of the node. The OCT imaging beam was incident from the back-side of the 3-D block in (**a**), and perpendicular to the 2-D OCT images shown above. The lymph node was translated in 10 μm increments in the X-Z plane to acquire each 2-D image comprising the 3-D data set. Pixel dimensions in the 3-D set are 1 μm, 10 μm, and 3 μm in the x, y, and z directions, respectively. Scale bars = 100 μm.

the adipose tissue in which the lymph node is embedded, and the nuclei of adipocytes, which are displaced to the edge of the cells by the central lipid collection. The OCT images in Figure 4 show many detailed internal structures including the capsule, a strong fibrous tissue enclosing the lymph node, the cortex, the outer part of the node containing dense masses of lymphocytes, and the medullary sinuses, the central section of the node composed of lymphoid elements with large sinusoids. All of these structures are strongly correlated with the H&E stained histological sections. During the initial *in vivo* imaging, the presence of motion artifacts due to cardiopulmonary activity was observed over the acquisition period. Due to the extended period of time needed to acquire 3-D data sets, OCT imaging was subsequently performed *in vitro*.

In this rat lymph node morphology imaging study, no significant differences were detected between the OCT images of lymph nodes from tumor-bearing animals and those from control animals. The H&E stained sections from these animals were examined by a board-certified pathologist in Veterinary Pathobiology to confirm that no micrometastases or isolated tumor cells were found in the rat lymph nodes.

For comparison with the previous normal-appearing lymph nodes, images were acquired from a late-stage metastatic human lymph node (Figures 5 and 6). The cervical lymph node specimen was resected from an 80-year-old female patient with Stage 4, T4N2b (53) squamous cell carcinoma of the oral cavity. Figure 5 shows a region infiltrated with tumor. The inhomogeneous scattering regions in the OCT images are a result of the destruction of the lymph node architecture, and contrast the optical scattering properties observed in the OCT images of normal nodes. Figure 6 shows regions of necrotic tumor tissue bordered by adipose tissue. Clear microstructural and cellular scattering differences are noted when compared with the normal lymph nodes in Figures 3 and 4.

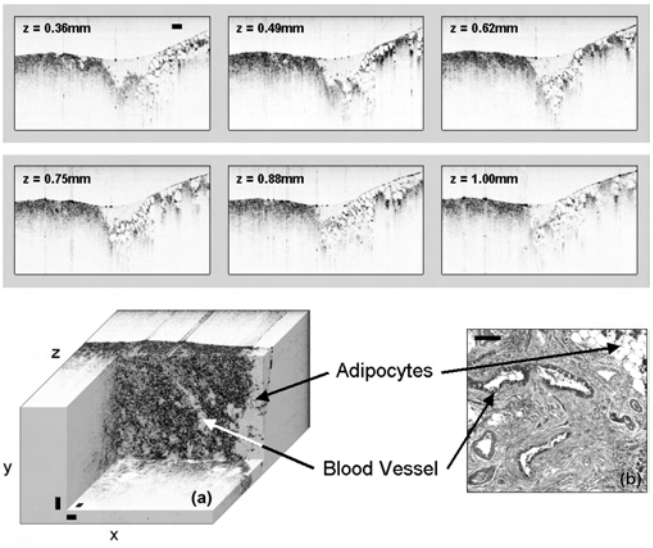

Figure 5: Images of a human lymph node with metastatic squamous cell carcinoma. *Top*: Sequence of 2-D OCT images through the node shows changing nodal boundary structure. The structure of blood vessels and the regions of squamous cell carcinoma are well correlated between OCT and H&E-stain histology images. (**a**) Computational cutout of a block extracted from the 3-D OCT data set. (**b**) Corresponding H&E-stained histological section of the lymph node. The OCT imaging beam was incident from the back-side of the 3-D block in (**a**), and from the top of the 2-D OCT images shown above. The lymph node was translated in 7 μm increments in the X-Z plane to acquire each 2-D image comprising the 3-D data set. Pixel dimensions in the 3-D set are 2 μm, 7 μm, and 3 μm in the x, y, and z directions, respectively. Scale bars = 100 μm.

Discussion

The results reported here represent the first demonstration of OCT imaging of lymph node morphology. The resulting images show the internal structures of the lymph nodes at a high resolution (2 μm axial, 15 μm transverse) and as deep as 1 mm in the highly scattering lymphatic tissue. The observed internal lymph node architecture is clearly identifiable when imaged from the external surface, and strongly correlated with corresponding histological observations, showing that lymph nodes are a promising target for clinical OCT application. Despite the depth penetration limits of

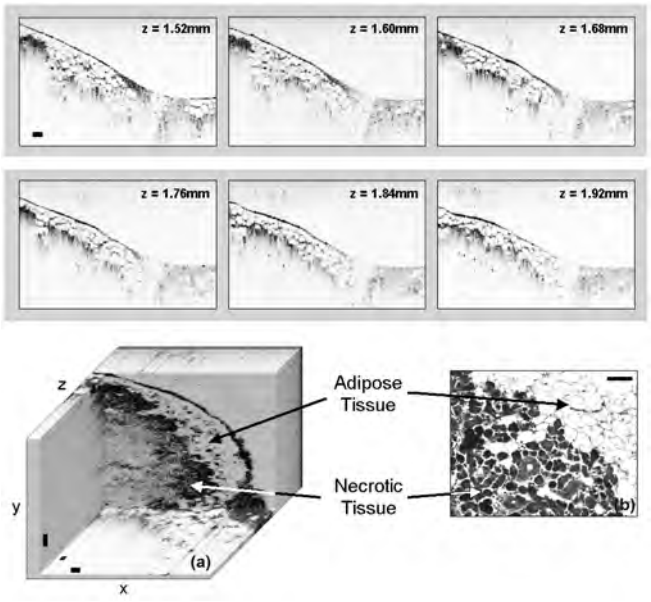

Figure 6: Images of a human lymph node with metastatic and necrotic squamous cell carcinoma. Regions of advanced necrosis are evident in both OCT and histology images. *Top*: Sequence of 2-D OCT images showing the changing lymph node boundary. (**a**) Computational cutout of a block extracted from the 3-D OCT data set. (**b**,**c**) Corresponding H&E-stained histological sections. The OCT imaging beam was incident from the back-side of the 3-D block in (**a**), and from the top of the 2-D OCT images shown above. The lymph node was translated in 8 μm increments in the X-Z plane to acquire each 2-D image comprising the 3-D data set. Pixel dimensions in the 3-D set are 2 μm, 8 μm, and 3 μm in the x, y, and z directions, respectively. Scale bars = 100 μm.

OCT imaging (typically 2-3 mm), this study shows that relevant features are accessible from the surface and that in many cases the entire node can be visualized given 3-D scanning. Reactive nodes increase significantly in size but also have larger reactive follicles near the surface, which are amenable to OCT imaging. The imaging depth in these highly-scattering nodes may also be extended by using light at a longer wavelength for OCT imaging. The 800 nm light used in this study also had an extremely broad spectral bandwidth, enabling the high axial imaging resolution. It is well known that longer wavelengths scatter less within the biological window of tissue. Therefore, deeper imaging penetration may be possible with the use of 1300 nm light, a second commonly used wavelength for OCT. However, achieving the high resolutions demonstrated in this study at the 1300 nm wavelength is currently a technical challenge being addressed in biomedical optics.

The Breast Committee of the American Joint Commission on Cancer (AJCC) proposed the classification of micrometastases as metastatic cell groupings smaller than 2.0 mm but larger than 0.2 mm (51). The size of detected micrometastases in the sentinel node is clinically relevant, potentially affecting node removal (54). With the demonstrated capability of detecting single nuclei on the order of 5 μm in size (Figure 3), OCT has the potential to detect micrometastases present within lymph nodes. While a single abnormal cell is unlikely to be differentiable from normal tissue due to its small size, clusters of abnormal cells may be evident. Tumor cells often exhibit nuclear enlargement, higher nuclear-to-cytoplasmic ratios, and pleomorphism, all changes that are likely to result in increased scattering that is detectable *via* OCT (55). While no micrometastases or isolated tumor cells were detected in the images from the animal model, this is likely due to non-metastatic growth rather than OCT imaging limitations. This is further substantiated by the lack of micrometastases and isolated tumor cells upon histopathological examination of H&E stained sections. We have shown, however, *via* images from late-stage metastatic disease in human lymph nodes, that these metastases can be clearly visualized with OCT, and that there is potential for the detection of micrometastases given further study.

While OCT images provide very high resolution due to the short wavelength of light, they also suffer from inherent attenuation effects due to the light scattering and absorption properties of tissue. These effects lead to an inherent tradeoff between the high resolution and the relatively shallow penetration depths of OCT imaging compared to other clinical imaging modalities. This tradeoff requires that minimally-invasive techniques be used for *in vivo* OCT imaging of sub-surface structures. Given an appropriate minimally-invasive OCT forward-imaging device such as those previously reported (41, 42), *in vivo* imaging is a feasible means by which to assess nodal structure without excision. Upon insertion of a needle probe similar to that in Figure 1 (inset), the incident beam can be rotated and translated about the needle tip, providing a 3-D data set of the surrounding internal lymph node architecture. Upon real-time evaluation of the OCT image, one can redirect the probe accordingly to the site of interest. This allows for the enhanced assessment of the node and potentially improved accuracy and precision in the removal of metastatic lymph nodes. Studies of *in vivo* catheter-based OCT imaging in cardiology have successfully demonstrated a similar technique used to evaluate plaque deposits (56) within coronary arteries.

The use of an intraoperative, high-resolution, real-time imaging technique would be highly advantageous due to the potential reduction in the number of necessary lymph node resections and the normal risks and side effects associated with any surgical procedure. Additionally, the elimination of the initial intermediate pathological evaluation provides physicians with real-time diagnostic information, reducing the time to diagnosis and the patient's stress while allowing for the immediate pursuit of appropriate treatment. The high acquisition rates afforded by the recent introduction of SD-OCT offer the potential to eliminate motion artifacts and thereby allow for improved *in vivo* imaging. Additionally, high speed image acquisition makes 3-D imaging more practical, thereby providing additional morphological information to the clinician.

In this paper, we have provided a brief description of the OCT technology and have demonstrated that OCT is capable of 3-D imaging of lymph node morphology with high resolution. Using computationally constructed 3-D OCT data sets, many detailed internal structures are easily identified including the lymphoid follicles, the cortex, the capsule, and the medullary sinuses. These features change in physical size and in their optical scattering properties when a lymph node becomes reactive or contains metastatic disease, as was evident in the images of the metastatic human lymph node. Future studies will investigate these changes in lymph nodes with histopathologically-evident micrometastases and isolated tumor cells. Given further study, OCT may become a powerful tool for the intraoperative evaluation and staging of metastatic breast cancer.

Acknowledgments

The authors acknowledge the technical assistance of Prof. Matthew Wallig, Veterinary Pathobiology Department, University of Illinois at Urbana-Champaign, and Dr. Robert Folberg, Department of Pathology, University of Illinois at Chicago. We also thank Prof. Keith Singletary of the Department of Nutrition for his assistance with our animal model, and the physicians at Carle Clinic Association and Carle Foundation Hospital, including Drs. Patricia Johnson

and Charles Wisseman. This work was supported in part by grants from the UIUC-UIC Intercampus Research Initiative in Biotechnology (S.A.B.) and the National Institutes of Health (NIBIB, 1 R01 EB00108-1, S.A.B.). Additional information can be found at http://biophotonics.uiuc.edu.

References

1. *Cancer Facts and Figures*, American Cancer Society (2005).
2. *Cancer Prevention and Early Detection Facts and Figures*, American Cancer Society (2005).
3. Estourgie, S. H., Nieweg, O. E., Olmos, R. A., Rutgers, E. J., Kroon, B. B. Lymphatic Drainage Patterns from the Breast. *Annals of Surgery 239*, 232-237 (2004).
4. Krag, D., Ashikaga, T., Harlow, S. P., Weaver, D. L. Development of Sentinal Node Targeting Technique in Breast Cancer Patients. *The Breast Journal 4*, 67-74 (1998).
5. Morton, D. L., Wen, D. R., Wong, J. H., Economou, J. S., Cagle, L. A., Storm, F. K., Foshag, L. J., Cochran, A. J. Technical Details of Intraoperative Lymphatic Mapping for Early Stage *Melanoma*. *Archives of Surgery 127*, 392-399 (1992).
6. Alex, J. C., Weaver, D. L., Fairbank, J. T., Rankin, B. S., Krag, D. N. Gamma-Probe-Guided Lymph Node Localization in Malignant Melanoma. *Surgical Oncology 2*, 303-308 (1993).
7. Veronesi, U., Paganelli, G., Viale, G., Luini, A., Zurrida, S., Galimberti, V., Intra, M., Veronesi, P., Robertson, C., Maisonneuve, P., Renne, G., De Cicco, C., De Lucia, F., Gennari, R. A Randomized Comparison of Sentinel-Node Biopsy with Routine Axillary Dissection in Breast Cancer. *New England Journal of Medicine 349*, 546-553 (2003).
8. Krag, D., Weaver, D., Ashikaga, T., Moffat, F., Klimberg, V. S., Shriver, C., Feldman, S., Kusminsky, R., Gadd, M., Kuhn, J., Harlow, S., Beitsch, P. The Sentinel Node in Breast Cancer – A Multicenter Validation Study. *New England Journal Medicine 339*, 941-946 (1998).
9. Kim, S., Lim, Y. T., Soltesz, E. G., Grand, A. M. D., Lee, J., Nakayama, A., Parker, J. A., Mihaljevic, T., Laurence, R. G., Dor, D. M., Cohn, L. H., Bawendi, M. G., Frangioni, J. V. Near-Infrared Fluorescent Type II Quantum Dots for Sentinel Lymph Node Mapping. *Nature Biotechnology 22*, 93-97 (2004).
10. Nimura, H., Narimiya, N., Mitsumori, N., Yamazaki, Y., Yanaga, K., Urashima, M. Infrared Ray Electronic Endoscopy Combined with Indocyanine Green Injection for Detection of Sentinel Nodes of Patients with Gastric Cancer. *British Journal of Surgery 91*, 575-579 (2004).
11. Kobayashi, H., Kawamoto, S., Sakai, Y., Choyke, P. L., Star, R. A., Brechbiel, M. W., Sato, N., Tagaya, Y., Morris, J. C., Waldmann, T. A. Lymphatic Drainage Imaging of Breast Cancer in Mice by Micro-Magnetic Resonance Lymphangiography using a Nano-Size Paramagnetic Contrast Agent. *Journal of the National Cancer Institute 96*, 703-708 (2004).
12. Huang, D., Swanson, E. A., Lin, C. P., Schuman, J. S., Stinson, W. G., Chang, W., Hee, M. R., Flotte, T., Gregory, K., Puliafito, C. A., Fujimoto, J. G. Optical Coherence Tomography. *Science 254*, 1178-1181 (1991).
13. Boppart, S. A., Bouma, B. E., Pitris, C., Southern, J. F., Brezinski, M. E., Fujimoto, J. G. *In Vivo* Cellular Optical Coherence Tomography Imaging. *Nature Medicine 4*, 861-865 (1998).
14. Brezinski, M. E., Tearney, G. J., Boppart, S. A., Swanson, E. A., Southern, J. F., Fujimoto, J. G. Optical Biopsy with Optical Coherence Tomography: Feasibility for Surgical Diagnostics. *Journal of Surgical Research 71*, 32-40 (1997).
15. Schuman, J. S., Puliafito, C. A. and Fujimoto, J. G. *Optical Coherence Tomography of Ocular Diseases*. Slack Inc., Thorofare, NJ (2004).
16. Schmitt, J. M., Knuttel, A., Yadlowsky, M., Eckhaus, M. A. Optical-Coherence Tomography of a Dense Tissue: Statistics of Attenuation and Backscattering. *Physics in Medicine and Biology 39*, 1705-1720 (1994).
17. Boulnois, J. L. Photophysical Processes in Recent Medical Laser Developments: A Review. *Lasers in Medical Science 1*, 47-66 (1986).
18. Profio, A. E., Doiron, D. R. Transport of Light in Tissue in Photodynamic Therapy. *Photochemistry and Photobiology 46*, 591-599 (1987).
19. Bechara, F. G., Gambichler, T., Stucker, M., Orlikov, A., Rotterdam, S., Altmeyer, P., Hoffmann, K. Histomorphologic Correlation with Routine Histology and Optical Coherence Tomography. *Skin Research and Technology 10*, 169-173 (2004).
20. Weissman, J., Hancewicz, T., Kaplan, P. Optical Coherence Tomography of Skin for Measurement of Epidermal Thickness by Shapelet-Based Image Analysis. *Optics Express 12*, 5760-5769 (2004).
21. Brezinski, M. E., Tearney, G. J., Bouma, B. E., Izatt, J. A., Hee, M. R., Swanson, E. A., Southern, J. F., Fujimoto, J. G. Optical Coherence Tomography for Optical Biopsy. Properties and Demonstration of Vascular Pathology. *Circulation 93*, 1206-1213 (1996).
22. Gerckens, U., Buellesfeld, L., McNamara, E., Grube, E. Optical Coherence Tomography (OCT) – Potential of a New High-Resolution Intracoronary Imaging Technique. *Herz 28*, 496-500 (2003).
23. Tearney, G. J., Jang, I. K., Kang, D. H., Aretz, H. T., Houser, S. L., Brady, T. J., Schlendorf, K., Shishkov, M., Bouma, B. E. Porcine Coronary Imaging *In Vivo* by Optical Coherence Tomography. *Acta Cardiologica 55*, 233-237 (2000).
24. Boppart, S. A., Brezinski, M. E., Pitris, C., Fujimoto, J. G. Optical Coherence Tomography for Neurosurgical Imaging of Human Intracortical Melanoma. *Neurosurgery 43*, 834-841 (1998).
25. Lazebnik, M., Marks, D. L., Potgieter, K., Gillette, R., Boppart, S. A. Functional Optical Coherence Tomography for Detecting Neural Activity Through Scattering Changes. *Optics Letters 28*, 1218-1220 (2003).
26. Escobar, P. F., Belinson, J. L., White, A., Shakhova, N. M., Feldchtein, F. I., Kareta, M. V., Gladkova, N. D. Diagnostic Efficacy of Optical Coherence Tomography in the Management of Preinvasive and Invasive Cancer of Uterine Cervix and Vulva. *International Journal of Gynecological Cancer 14*, 470-474 (2004).
27. Pitris, C., Goodman, A., Boppart, S. A., Libus, J. J., Fujimoto, J. G., Brezinski, M. E. High-Resolution Imaging of Gynecologic Neoplasms using Optical Coherence Tomography. *Obstetrics and Gynecology 93*, 135-139 (1999).
28. Brand, S., Poneros, J. M., Bouma, B. E., Tearney, G. J., Compton, C. C., Nishioka, N. S. Optical Coherence Tomography in the Gastrointestinal Tract. *Endoscopy 32*, 796-803 (2000).
29. Tearney, G. J., Brezinski, M. E., Southern, J. F., Bouma, B. E., Boppart, S. A., Fujimoto, J. G. Optical Biopsy in Human Gastrointestinal Tissue using Optical Coherence Tomography. *American Journal of Gastroenterology 92*, 1800-1804 (1997).
30. Drexler, W. Ultrahigh-Resolution Optical Coherence Tomography. *Journal of Biomedical Optics 9*, 47-74 (2004).
31. Bouma, B. E., Tearney, G. J., Boppart, S. A., Hee, M. R., Brezinski, M. E., Fujimoto, J. G. High Resolution Optical Coherence Tomographic Imaging using a Modelocked Ti:Al2O3 Laser. *Optics Letters 20*, 1486-1488 (1995).
32. Povazay, B., Bizheva, K., Unterhuber, A., Hermann, B., Sallmann, H., Fercher, A. F., Drexler, W., Apolonski, A., Wadsworth, W. J., Knight, J. C., Russell, P. S. J., Vetterlein, M., Scherzer, E. Submicrometer Axial Resolution Optical Coherence Tomography. *Optics Letters 27*, 1800-1802 (2002).
33. Fercher, A. F., Hitzenberger, C. K., Kamp, G., El-Zaiat, S. Y. Measurement of Intraocular Distances by Backscattering Spectral Interferometry. *Optics Communications 117*, 43-48 (1995).

34. Yun, S. H., Tearney, G. J., Bouma, B. E., Park, B. H., de Boer, J. F. High-Speed Spectral Domain Optical Coherence Tomography at 1.3 μm Wavelength. *Optics Express 11*, 3598-3604 (2003).
35. Nassif, N., Cense, B., Park, B., Pierce, M., Yun, S., Bouma, B., Tearney, G., Chen, T., de Boer, J. *In Vivo* High-Resolution Video-Rate Spectral-Domain Optical Coherence Tomography of the Human Retina and Optic Nerve. *Optics Express 12*, 367-376 (2004).
36. Schaefer, A. W., Reynolds, J. J., Marks, D. L., Boppart, S. A. Real-Time Digital Signal Processing-Based Optical Coherence Tomography and Doppler Optical Coherence Tomography. *IEEE Transactions on Biomedical Engineering 51*, 186-190 (2004).
37. Wong, R. C., Yazdanfar, S., Izatt, J. A., Kulkarni, M. D., Barton, J. K., Welch, A. J., Willis, J., Sivak, M. V., Jr. Visualization of Subsurface Blood Vessels by Color Doppler Optical Coherence Tomography in Rats: Before and After Hemostatic Therapy. *Gastrointestinal Endoscopy 55*, 88-95 (2002).
38. de Boer, J. F., Milner, T. E. Review of Polarization Sensitive Optical Coherence Tomography and Stokes Vector Determination. *Journal of Biomedical Optics 7*, 359-371 (2002).
39. Oldenburg, A. L., Gunther, J. R. and Boppart, S. A. Imaging Magnetically Labeled Cells with Magnetomotive Optical Coherence Tomography. *Optics Letters 30*, 747-749 (2005).
40. Xu, C., Ye, J., Marks, D. L., Boppart, S. A. Near-Infrared Dyes as Contrast-Enhancing Agents for Spectroscopic Optical Coherence Tomography. *Optics Letters 29*, 1647-1649 (2004).
41. Boppart, S. A., Bouma, B. E., Pitris, C., Fujimoto, J. Forward-Imaging Instruments for Optical Coherence Tomography. *Optics Letters 22*, 1618-1620 (1998).
42. Li, X., Chudoba, C., Ko, T., Pitris, C., Fujimoto, J. Imaging Needle for Optical Coherence Tomography. *Optics Letters 25*, 1520-1522 (2000).
43. Boppart, S. A., Luo, W., Marks, D. L., Singletary, K. W. Optical Coherence Tomography: Feasibility for Basic Research and Image-Guided Surgery of Breast Cancer. *Breast Cancer Research and Treatment 84*, 85-97 (2004).
44. Gullino, P. M., Pettigrew, H. M., Grantham, F. H. N-Nitrosomethylurea as Mammary Gland Carcinogen in Rats. *Journal of the National Cancer Institute 54*, 401-414 (1975).
45. Russo, J., Russo, I. H., van Zwieten, M. J., Rogers, A. E., Gusterson, B. Classification of Neoplastic and Non-Neoplastic Lesions of the Rat Mammary Gland, In *Integument and Mammary Glands, Monographs on Pathology of Laboratory Animals*. Eds., Jones, T. C., Mohr U., Hunt R. D. Springer Verlag, Berlin, Germany (1989).
46. Thordarson, G., Lee, A. V., McCarty, M., Van Horn, K., Chu, O., Chou, Y. C., Yang, J., Guzman, R. C., Nandi, S., Talamantes, F. Growth and Characterization of N-Methyl-N-Nitrosourea-Induced Mammary Tumors in Intact and Ovariectomized Rats. *Carcinogenesis 22*, 2039-2047 (2001).
47. Thompson, H. J., Singh, M., McGinley, J. Classification of Premalignant and Malignant Lesions Developing in the Rat Mammary Gland after Injection of Sexually Immature Rats with L-Methyl-L-Nitrosourea. *Journal of Mammary Gland Biology and Neoplasia 5*, 201-210 (2000).
48. McCormick, D. L., Adamowski, C. B., Fiks, A., Moon, R. C. Lifetime Dose-Response Relationships for Mammary Tumor Induction by a Single Administration of N-Methyl-N-Nitrosourea. *Cancer Research 41*, 1690-1694 (1981).
49. Tavassoli, F. A. *Pathology of the Breast*. Elselvier, New York (1992).
50. Arafah, B. M., Finegan, H. M., Roe, J., Manni, A., Pearson, O. H. Hormone Dependency in N-Nitrosomethylurea-Induced Rat Mammary Tumors. *Endocrinology 111*, 584-588 (1982).
51. Tjan-Heijnen, V. C., Buit, P., de Widt-Evert, L. M., Ruers, T. J., Beex, L. V. Micro-Metastases in Axillary Lymph Nodes: An Increasing Classification and Treatment Dilemma in Breast Cancer Due to the Introduction of the Sentinel Lymph Node Procedure. *Breast Cancer Research and Treatment 70*, 81-88 (2001).
52. Podoleanu, A. G. Unbalanced Versus Balanced Operation in an Optical Coherence Tomography System. *Applied Optics 39*, 173-182 (2000).
53. *Collaborative Staging Manual and Coding Instructions*, National Institutes of Health, Publication Number 04-5496 (2004).
54. Rutledge, H., Davis, J., Chiu, R., Cibull, M., Brill, Y., McGrath, P., Samayoa, L. Sentinel Node Micrometastasis in Breast Carcinoma May Not be an Indication for Complete Axillary Dissection. *Modern Pathology 18*, 762-768 (2005).
55. Mourant, J. R., Canpolat, M., Brocker, C., Esponda-Ramos, O., Johnson, T. M., Matanock, A., Stetter, K., Freyer, J. P. Light Scattering from Cells: The Contribution of the Nucleus and the Effects of Proliferative Status. *Journal of Biomedical Optics 5*, 131-137 (2000).
56. Jang, I. K., Tearney, G. J., MacNeill, B., Takano, M., Moselewski, F., Iftima, N., Shishkov, M., Houser, S., Aretz, H. T., Halpern, E. F., Bouma, B. E. *In Vivo* Characterization of Coronary Atherosclerotic Plaque by use of Optical Coherence Tomography. *Circulation 111*, 1551-1555 (2005).

Date Received: May 31, 2005
Date Accepted: August 5, 2005